Realizing Shape and Size Control for the Synthesis of Coordination Polymer Nanoparticles templated by Diblock Copolymer Micelles

Christoph Göbel,[a] Katharina Marquardt[†,b] Dirk Baabe,[c] Markus Drechsler,[d] Patrick Loch,[e] Josef Breu,[e] Andreas Greiner,[f] Holger Schmalz,[f] and Birgit Weber*[a]

[a.] *Department of Chemistry, Inorganic Chemistry IV, Universität Bayreuth, Universitätsstr. 30, 95447 Bayreuth, Germany*.
[b.] *Bavarian Research Institute of Experimental Geochemistry and Geophysics (BGI), Universität Bayreuth, Universitätsstr. 30, 95447 Bayreuth, Germany.*
[c.] *Institut für Anorganische und Analytische Chemie, Technische Universität Braunschweig, Hagenring 30, 38106 Braunschweig, Germany*
[d.] *Keylab Electron and Optical Microscopy, Bavarian Polymer Institute, Universität Bayreuth, Universitätsstr. 30, 95447 Bayreuth, Germany*
[e.] *Department of Chemistry, Inorganic Chemistry I, Universität Bayreuth, Universitätsstr. 30, 95447 Bayreuth, Germany*
[f.] *Department of Chemistry, Macromolecular Chemistry II and Keylab Synthesis and Molecular Characterization, Bavarian Polymer Institute, Universität Bayreuth, Universitätsstr. 30, 95447 Bayreuth, Germany*

† Dr. K. Marquardt, Imperial College London, Department of Materials, Royal School of Mines Exhibition Road, London, SW7 2AZ – UK..

Electronic Supplementary Information (ESI) available: all details on the characterization of the dBCPs (NMR spectroscopy, GPC, DSC and DLS) and of the SCO-CP-dBCP nanocomposites (TEM, DLS, IR spectroscopy, PXRD, Mössbauer spectroscopy, SQUID magnetometry). Supporting Information for this article is given via a link at the end of the document.

Abstract

The combination of polymers with nanoparticles offers the possibility to obtain customizable composite materials with additional properties such as sensing or bistability provided by a switchable spin crossover (SCO) core. For all applications, a precise control over size and shape of the nanomaterial is highly important as it will significantly influence its final properties. By confined synthesis of iron(II) SCO coordination polymers within the P4VP cores of polystyrene-*block*-poly-4-vinylpyridine (PS-*b*-P4VP) micelles in THF we are able to control the size and also the shape of the resulting SCO nanocomposite particles by the composition of the PS-*b*-P4VP diblock copolymers (dBCPs) and the amount of complex employed. For the nanocomposite samples with the highest P4VP content, a morphological transition from spherical nanoparticle to worm-like structures was observed with increasing coordination polymer content, which can be explained with the impact of complex coordination on the self-assembly of the dBCP. Furthermore, the SCO nanocomposites showed transition temperatures of $T_{1/2}$ = 217 K, up to 27 K wide hysteresis loops and a decrease of the residual high-spin fraction down to γ_{HS} = 14% in the worm-like structures, as determined by magnetic susceptibility measurements and Mössbauer spectroscopy. Thus, SCO properties close or even better (hysteresis) to those of the bulk material can be obtained and furthermore tuned through size and shape control realized by tailoring the block length ratio of the PS-*b*-P4VP dBCPs.

Introduction

The synthesis of nanomaterials with well-defined size and shape is one of the cornerstones of nanotechnology. The step from the bulk material to nanoscale is important for a wide range of applications, which is either due to size-dependent properties, large surface areas or a better processablity.[1–3] A well-known example for size and shape dependent properties is the plasmon resonance of nanoparticles of materials with delocalized electronic states. [4,5] In case of catalytically active particles, size reduction ensures large surface areas and by this high catalytic activity. Besides the established effects of size, examples for a shape dependent activity are also known, e.g. due to different number of under–coordinated atoms depending on the shape of Pt nanoparticles[6] or quantum confinement effects in heterostructures.[7] Another notable example for shape-dependent properties are calcium-alginate hydrogels containing polylactide nanoparticles. Here the shape of the nanoparticles has a significant impact on the final adhesive and mechanical properties of the composite material.[8]

For functional materials, nanosized particles are often necessary for an implementation of the material into devices. With regard to application, spin crossover (SCO) complexes are a highly promising family of functional materials because of their unique switching properties by different external stimuli (e.g. temperature, pressure or light irradiation) between a high-spin (HS) and a low-spin (LS) state.[9] Switching between these two states changes

physical properties like magnetism, structure, or color.[10] This offers interesting applications, *e.g.* as sensors,[11] display devices and data storage,[12] contrast agents[13,14] or molecular actuators.[15,16] Here, it is a major obstacle of current research to maintain bulk properties down to very small particle sizes.[17–19]

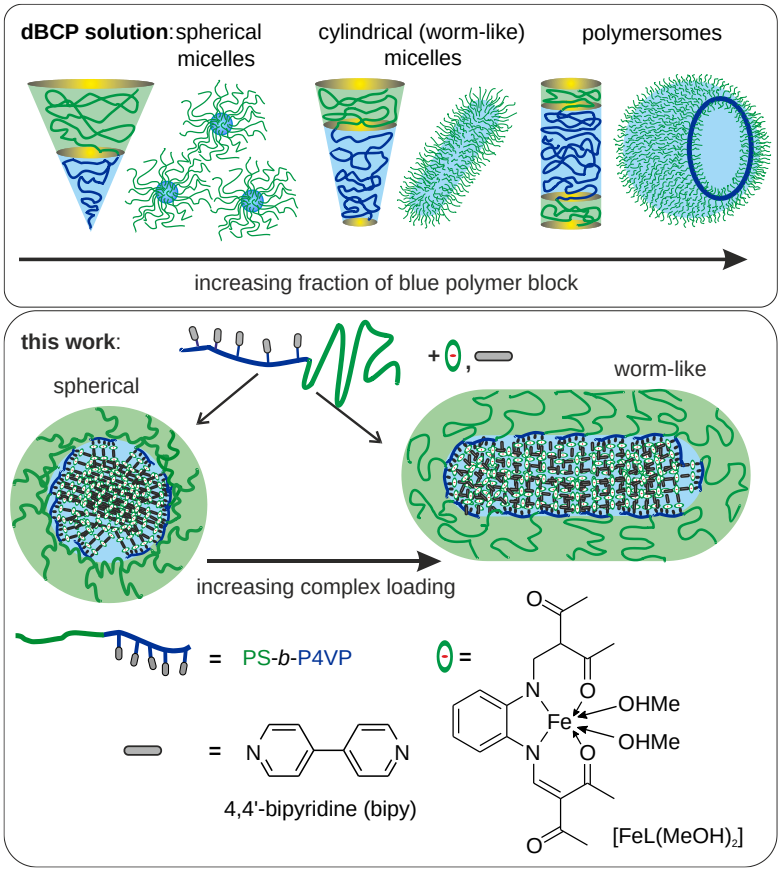

Scheme 1. Top: Structures obtained by self-assembly of diblock copolymers as function of the volume fraction of the two polymer blocks in a selective solvent for the green block. Bottom: Desired nanocomposite particle structures produced by self-assembly of PS-*b*-P4VP dBCPs in the presence of SCO complexes in THF as selective solvent, including the used abbreviations

As the SCO properties strongly depend on the crystal packing, typically an increasing residual HS fraction, a decreasing hysteresis width, and a shift of the transition temperature to lower temperatures is observed for decreasing particle sizes.[18,20–22] However, next to size also the shape of particles can be important either for the resulting spin crossover properties,[23] or for the implementation into devices.[24] For applications as molecular actuators,[16,25,26] for example, nanosized rod-like structures are desirable to realize an anisotropic volume expansion. To date, it is still challenging to synthesize nanoparticles or nanocomposites with shapes different from those observed for the bulk material or spherical ones.[27,28] This applies in particular for nanoparticles of coordination polymers or networks. Here, the inverse micelle technique or fast precipitation methods are the most established methods that usually yield spherical nanoparticles or nano-crystallites with shapes close to those observed for the bulk material.[19,29,30]

The aim of the work presented here is to employ diblock copolymer (dBCP) micelles, whose shape and size can be easily tailored by composition and overall molecular weight, as nanoreactors for the synthesis of spin crossover coordination polymer nanocomposites. As illustrated in the top of Scheme1, the volume fraction of the two polymer blocks of dBCPs defines the micelle morphology obtained by self-assembly in a selective solvent for one of the blocks.[31–33] This enables their use as micro- or nanoreactors for the synthesis of nanoparticles.[34–40] Moreover, the formation of polymer-encapsulated composite materials promises simple processing by established methods like electrospinning for the formation of fibers and fiber mats[41–45] or spin-coating and drop-casting for surface coating.[46,47] In this context, recent studies of SCO nanomaterials by us and others have shown that the introduction of coating and interfaces influences the SCO behavior and conversely, how this interaction can be exploited to trigger new functionalities.[17,48,49,50,51]

Recently we showed the potential of polystyrene-*block*-poly(4-vinylpyridine) (PS-*b*-P4VP) diblock copolymer micelles as nanoreactors for the synthesis of spherical coordination polymer[52,17,53] or networks nanoparticles.[54] Here we address, if a systematic increase in the P4VP fraction can be used to control not only the size, but also the morphology of the obtained nanocomposites. Furthermore, the encapsulation of the coordination polymer could further influence the self-assembly properties of the dBCP in solution (Scheme 1, bottom). As a result of this approach, we herein report for the first time not only a very precise size control, but also shape control for such CP-dBCP nanocomposites based on spin crossover complexes.

Results and discussion

Characterization of PS-*b*-P4VP dBCP Micelles

Five different dBCPs with a target molecular weight between 120 000 g mol^{-1} and 160 000 g mol^{-1} have been successfully synthesized with P4VP fractions ranging from 15 wt% (SV-15) to 61 wt% (SV-61). The composition, used abbreviations, number average molecular weights (M_n) and dispersities ($Đ$) are given in **Table 1**. The general characterization of the dBCPs by proton nuclear magnetic resonance (^{1}H-NMR) spectroscopy, gel permeation chromatography (GPC), differential scanning calorimetry (DSC) and dynamic light scattering (DLS) is summarized in **Figure S1** - **S4**.

In solution, THF is a very good solvent for the PS block, while the solubility of P4VP is quite low.[55] For PS-*b*-P4VP dBCPs with a notably lower P4VP fraction with respect to that of the soluble PS block, spherical micelles with an insoluble P4VP core and a soluble corona made of PS blocks will be formed.[56–62] Raising the fraction of the less soluble P4VP block alters the packing parameter of the dBCP chains, which can lead to a morphological transition to rods, worm-like micelles, or vesicles (top of **Scheme 1**).[63] The size and shape of the micelles formed by the five new diblock copolymers were characterized both in the dry state and in THF dispersion by TEM, DLS, and cryo-TEM. It is expected that they only show spherical micelles since the P4VP part is still too small (< 80%) for the formation of rods or worm-like micelles.[64] Due to the higher contrast, the crystalline P4VP core appears dark in the TEM pictures in **Figure 1** and **Figure S5** with the PS shell in light gray. In fact, only spherical micelles were found by TEM measurements for all dBCPs. The diameter of the insoluble P4VP cores (D_{core}) of the micelles increases continuously starting at 15 nm ± 2 nm for SV-15 and reaching 73 nm ± 9 nm for SV-61 (**Table 2** and **Figure 2A**). In addition, narrow hydrodynamic diameter distributions were detected for all diblock copolymer micelles by DLS (**Figure S4**). At first, the measured hydrodynamic diameters (D_h) of the dBCPs correlate with both the molecular weight and the P4VP fraction. The hydrodynamic diameters start at 75 nm ± 28 nm for SV-15 and increase with the P4VP fraction up to 125 nm ± 34 nm for SV-42. Although having the highest molecular weight and P4VP content of all analyzed dBCPs, SV-61 does not show the largest hydrodynamic diameter. Instead, it is similar to SV-42 with 119 nm ± 29 nm (**Figure S4** and **Figure 2A**), which can be explained with the reduced PS chain length, which also influences D_h.[57] The dBCPs were also imaged by cryo-TEM to evaluate the micelle size and shape in solution, which is important for their use as nanoreactor. Please note, due to the higher electron density contrast of the insoluble P4VP core, the soluble PS corona is hardly visible. Again, spherical micelles were found for all five neat dBCPs and diameters ranging from 26 nm ± 2 nm for SV-15 to 71 nm ± 4 nm for SV-61 were measured (**Table 2**). For the dBCP micelles with lower P4VP fractions (lower degree of polymerization of the P4VP block) the partial swelling of the core in THF is more pronounced leading to larger core diameters compared to the dried state. In **Figure 2A** the three diameters D_h, D_{core} and D_{cryo} are plotted vs. the P4VP fraction revealing the almost linear correlation for all three parameters.

Table 1. Molecular characteristics of the used diblock copolymers.

dBCP[a)]	Abbreviation	M_n [g mol^{-1}][b)]	$Đ$[c)]	Fraction PS [wt%][d)]	styrene units	Fraction P4VP [wt%][d)]	4VP units
$S_{85}V_{15}^{154}$	SV-15	154 000	1.02	85	1247	15	220
$S_{79}V_{21}^{119}$	SV-21	119 000	1.05	79	895	21	238
$S_{65}V_{35}^{131}$	SV-35	131 000	1.06	65	811	35	437
$S_{58}V_{42}^{157}$	SV-42	157 000	1.09	58	867	42	628
$S_{39}V_{61}^{162}$	SV-61	162 000	1.24	39	602	61	941

a) Subscripts denote the content of the respective block in wt%, superscript gives the number average molecular weight in kg mol^{-1}; b) calculated from ^{1}H-NMR measurements utilizing the absolute molecular weight of the PS precursor derived from MALDI-ToF MS; c) determined by DMF-GPC calibrated with narrowly distributed PS standards (Figure S2); d) calculated from ^{1}H-NMR measurements (for an exemplary calculation see Figure S1).

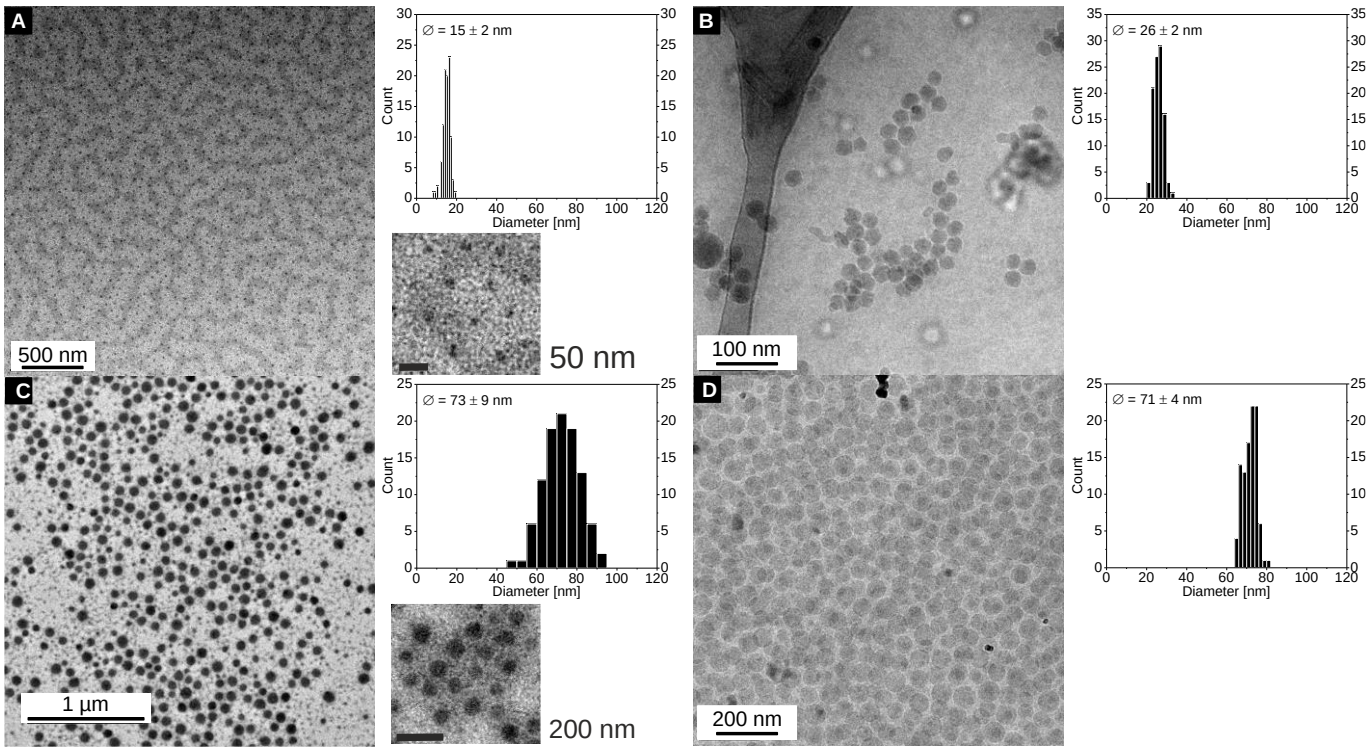

Figure 1. TEM (left) and cryo-TEM (right) images of micelles formed by the dBCPs SV-15 (A, B) and SV-61 (C, D) in THF (c = 2.5 g L^{-1})). The corresponding images for the dBCPs SV-21, SV-35 and SV-42 are given in the SI, Figure S5. Only spherical micelles were observed for all neat dBCPs. The corresponding P4VP core size distributions are given on the right.

Synthesis of SCO CP-dBCP nanocomposites.

25 different SCO CP-dBCP nanocomposites have been prepared utilizing the five before mentioned dBCPs through the incorporation of a SCO CP employing a different number of reaction cycles (5 samples each). A complete sample overview is given in **Table 2**. The reaction procedure is as follows: The diblock copolymer and the iron(II) complex [FeL(MeOH)$_2$] were dissolved in THF and heated to reflux for 2 h. After cooling, the bridging ligand 4,4'-bipyridine (bipy) was added and the reaction mixture was refluxed for another 1 h. At this stage, the solvent was either removed by cold distillation to yield a brown solid (1 cycle), or up to four additional cycles of simultaneous addition of the iron(II) complex and the bridging ligand and a subsequent heating to reflux for 1 h followed. Thus, nanocomposites with 3 to 5 cycles have been prepared. The numbers **1** to **5** of the sample notation correspond to the used dBCP, while the cycle count (1, 3, 4, and 5) is denoted by the letters **a** to **d**. Additionally, samples with five cycles were prepared with a reduced amount of the bridging ligand bipy to investigate the impact of the ligand excess on the confined coordination polymer formation. Please note that for the bulk material no impact of the bipy excess on the magnetic properties was observed,[65,66] but for the nanocomposite particles this might be different. These samples are labeled with the letter **e**. The influence of the incorporation of the CP on the size and shape of the nanocomposite particles in comparison to the neat PS-*b*-P4VP micelles was investigated by TEM, cryo-TEM, and DLS, whereas the influence of the different particle sizes and shapes on the magnetic properties was analyzed by magnetic susceptibility measurements and (temperature-dependent) ^{57}Fe Mössbauer spectroscopy. Further characterization was performed by (temperature-dependent) powder X-ray diffraction ((*T*-)PXRD), scanning electron microscopy (SEM), elemental analysis, and infrared (IR) spectroscopy. The detailed characterization of the samples **1–5e** is given in the following as typical representatives, while the characterization of the samples **1a-d**, **2a-d**, **3a-d**, **4a-d**, and **5a-d** is given in the Supporting Information.

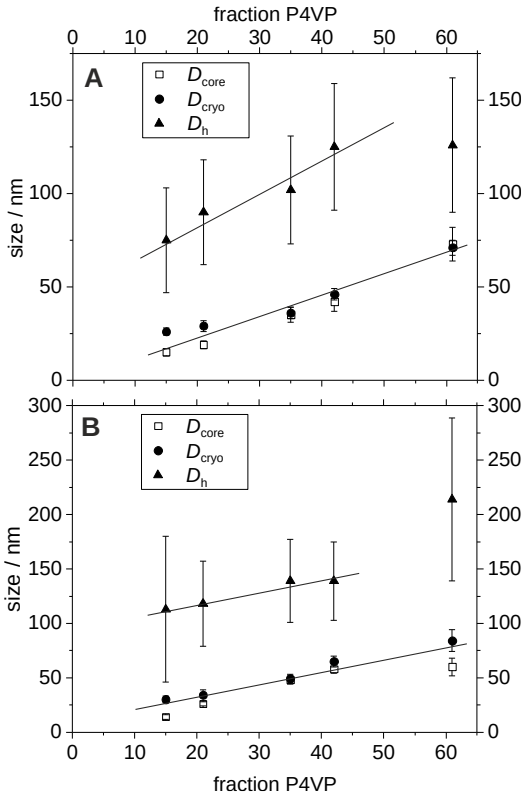

Figure 2. Plot of the hydrodynamic diameter (D_h) measured by DLS and core diameter derived from TEM (D_{core}) and cryo-TEM (D_{cryo}) measurements vs. the P4VP fraction for the 5 different dBCPs (A) and the 5 nanocomposites **1**–**5e** (B). The solid line is a guide for the eye only to illustrate the almost linear correlation for both series.

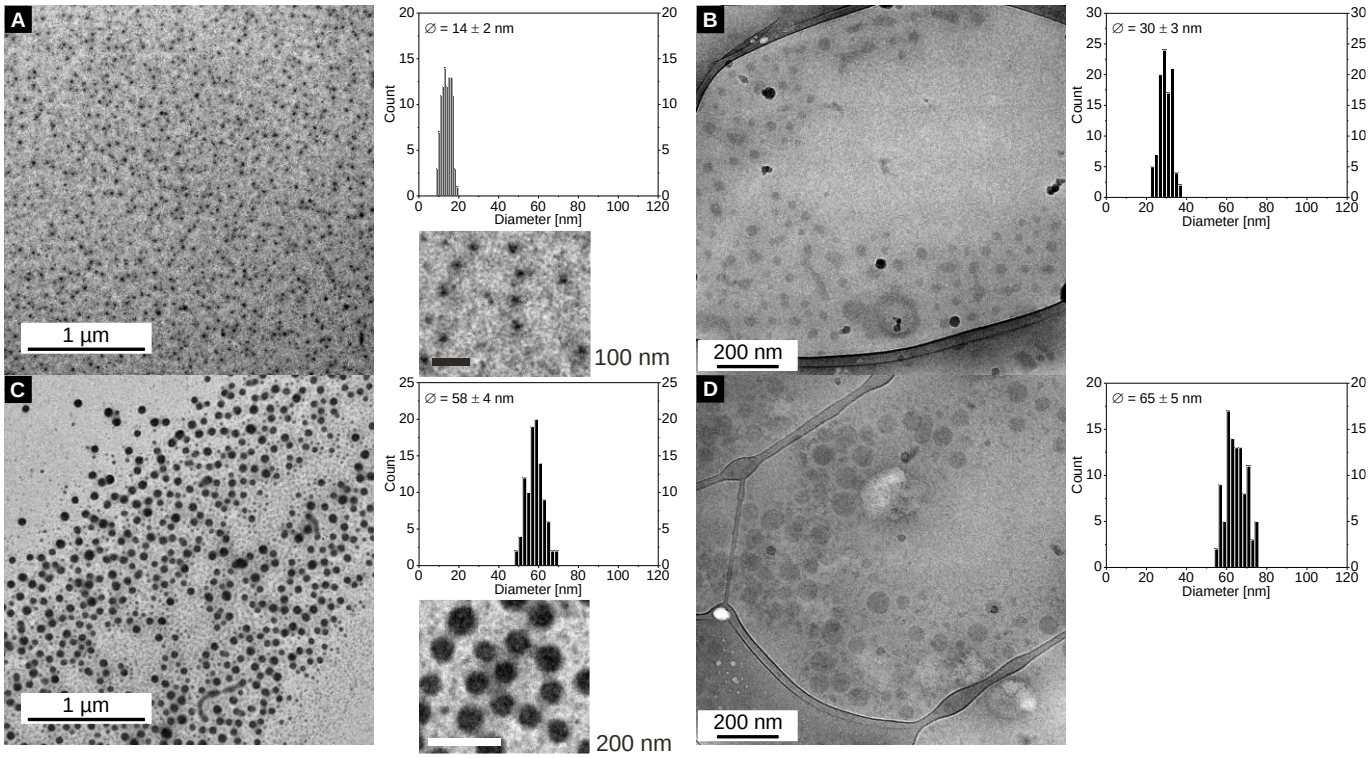

Figure 3. TEM (left) and cryo-TEM (right) micrographs of the SCO CP-dBCP nanocomposite particles **1e** (A, B) and **4e** (C, D) that show spherical nanoparticles in both characterization methods. The corresponding images for the **2e** and **3e** are given in the SI, Figure S10.The size distributions are given on the right.

Table 2. Overview of the hydrodynamic diameter (D_h) measured by DLS and core diameter (D_{core}) derived from TEM and cryo-TEM measurements of the 5 different dBCPs and the as-synthesized nanocomposite particles.

Sample	dBCP	Number of cycles	Shape (TEM)	Hydrodynamic diameter D_h (DLS) [nm]	Core diameter D_{core} (TEM) [nm]	Core diameter D_{cryo} (cryo-TEM) [nm]
	SV-15	-	spherical	75 ± 28	15 ± 2	26 ± 2
	SV-21	-	spherical	90 ± 28	19 ± 2	29 ± 3
	SV-35	-	spherical	102 ± 29	35 ± 4	36 ± 3
	SV-42	-	spherical	125 ± 34	42 ± 5	46 ± 3
	SV-61	-	spherical	126 ± 36	73 ± 9	71 ± 4
1a	SV-15	1	spherical	85 ± 33	12 ± 2	
1b	SV-15	3	spherical	89 ± 32	15 ± 3	-
1c	SV-15	4	spherical	121 ± 43	17 ± 2	-
1d	SV-15	5	spherical	119 ± 62	16 ± 2	-
1e[a)]	SV-15	5	spherical	113 ± 67	14 ± 2	30 ± 3
2a	SV-21	1	spherical	99 ± 33	23 ± 2	-
2b	SV-21	3	spherical	113 ± 34	26 ± 3	-
2c	SV-21	4	spherical	116 ± 36	26 ± 3	-
2d	SV-21	5	spherical	125 ± 38	26 ± 3	-
2e [a)]	SV-21	5	spherical	118 ± 39	26 ± 2	34 ± 5
3a	SV-35	1	spherical	112 ± 32	37 ± 3	-
3b	SV-35	3	spherical	125 ± 34	41 ± 4	-
3c	SV-35	4	spherical	112 ± 32	40 ± 3	-
3d	SV-35	5	spherical	131 ± 39	40 ± 3	-
3e [a)]	SV-35	5	spherical	139 ± 38	48 ± 4	49 ± 6
4a	SV-42	1	spherical	131 ± 34	53 ± 5	-
4b	SV-42	3	spherical	146 ± 46	52 ± 5	-
4c	SV-42	4	spherical	168 ± 57	53 ± 4	-
4d	SV-42	5	spherical	153 ± 46	53 ± 4	-
4e [a)]	SV-42	5	spherical	139 ± 36	58 ± 4	65 ± 5
5a	SV-61	1	spherical	129 ± 33	61 ± 7	-
5b	SV-61	3	spherical/rods	260 ± 113	62 ± 9	-
5c	SV-61	4	rods	218 ± 78	58 ± 7	-
5d	SV-61	5	rods/worm	-	56 ± 6	-
5e [a)]	SV-61	5	rods/worm	214 ± 75	60 ± 8	84 ± 10

a) Samples were also characterized by TEM, DLS, and SEM after thermal annealing (see Table S5).

Characterization of SCO CP-dBCP nanocomposite particles

SIZE AND SHAPE

The particle shape, D_{core} and D_h were determined for all SCO CP-dBCP nanocomposite particles by TEM and DLS, respectively. The particle shape and core diameters (D_{cryo}) in solution were further analyzed by cryo-TEM for the samples **1**–**5e**. As the SCO CP in the dBCP core has the highest electron density it appears black in TEM and cryo-TEM, whereas the PS corona is visible in light grey in TEM and not visible in cryo-TEM due to a lack in electron density contrast with respect to the vitrified THF matrix. The 20 samples **1-4, a-e** all show spherical nanocomposite particles in TEM measurements (**Figure 3** and **Figures S6-S10**). The average core diameter D_{core} increases continuously with rising P4VP fraction from 14 nm ± 2 nm (**1e**) to 58 nm ± 4 nm (**4e**) (see **Table 2** and **Figure 2B**). Furthermore, the core diameter of the nanocomposite samples does not change significantly with an increased cycle count. It is also independent of the used bipy excess during the synthesis, as determined by comparison of samples **d** and **e**. Cryo-TEM measurements also reflect the growth in the core sizes with increasing P4VP content. In line with the TEM measurements, spherical particles were observed for the SCO CP-dBCP nanocomposite samples **1-4e,** showing also slightly larger core diameters than the empty dBCPs. The hydrodynamic diameters D_h of the nanocomposite particles, analyzed by DLS, increased along the series from 113 nm ± 67 nm (**1e**) to 139 nm ± 36 nm (**4e**) (**Table 2** and **Figures S11**-**S15**). It is observed that the hydrodynamic diameter slightly increases with a higher cycle count, which may be an effect of the crystallization of the CP inside

the dBCPs core. In addition, the hydrodynamic diameter of the SCO CP-dBCP nanocomposite particles is significantly larger than the empty dBCP micelles. For the empty micelles the P4VP chains build the core. Upon addition of the coordination polymer the inner core is now formed by the complex that is surrounded by the P4VP chains. This most likely leads to an increased density of the P4VP chains on the surfaces and by this an increased stretching of the PS polymer chains and, thus, a larger hydrodynamic diameter (see **Figure S4** and **Figures S11**-**S15**). This effect diminishes in the composite particles when going from SV-15 to SV-42 because of the shorter PS chains.

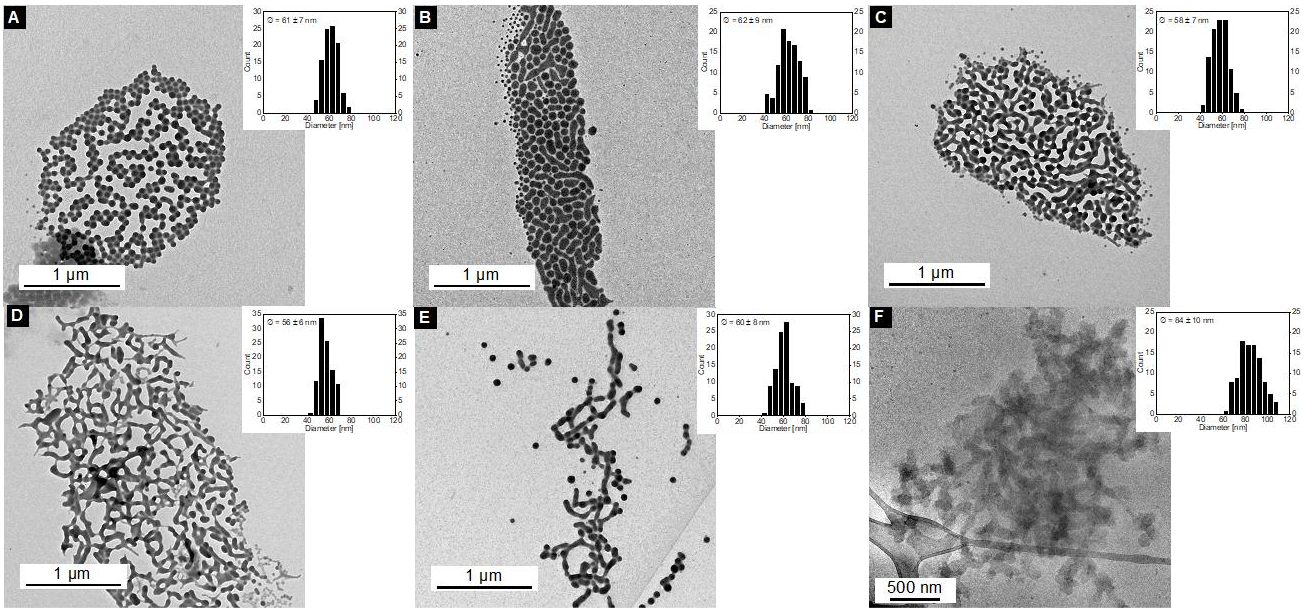

Figure 4. TEM micrographs of SCO CP-dBCP samples **5a** (A), **5b** (B), **5c** (C), **5d** (D) and **5e** (E) visualizing the transformation from spheres to worm-like nanocomposite particles. Cryo-TEM confirms the presence of worm-like micelles in solution for sample **5e** (F). The corresponding size distributions are given in the insets.

Interestingly, worm-like structures next to spherical particles were observed in nanocomposite particles with SV-61. While the nanocomposite particles **5a** are still spherical as are the empty dBCP micelles, worm-like structures started to form with sample **5b**, as shown in TEM and cryo-TEM measurements in **Figure 4**. The worm-like structures become predominant in samples **5c** and **5d** (**Figure 4**). D_{cryo} of both, the spherical nanocomposite particles and the worm-like structures, are also marginally larger than the spherical particle cores observed for the neat dBCP (71 nm ± 4 nm (SV-61) vs. 84 nm ± 10 nm (**5e**)), in line with the other samples discussed here (**Table 2**). However, D_{core} (micelle width) of those worm-like structures determined by TEM in sample **5e** with 60 nm ± 8 nm remained nearly identical to the particle size of sample **4e** (see **Figure 2B**). The formation of rods in samples **5b–e** is also indicated in the DLS measurements by the shift of the apparent size distribution to increasing particles sizes and an accompanied broadening of the size distribution, which is caused by the movement of the anisotropic rods/worms in solution (**Figure S15**). In **Figure 2B**, the three diameters D_h, D_{core} and D_{cryo} of the nanocomposites **1–5e** are plotted vs. the P4VP fraction. The sudden increase of D_h is clearly visible in comparison with the other samples. The formation of rods or worm-like structures in samples **5b-e** is in contrast to the formation of only spherical particles in the neat polymer SV-61 and can be explained by considering the weight fractions of the soluble (PS) and the less soluble or insoluble parts (P4VP and CP) of the resulting nanocomposites. Due to the introduction of the CP into the P4VP core, the weight fraction of the insoluble core increases. Exemplarily, a calculation of the weight fraction of these parts is given for sample **5e** by adding up the weight of the P4VP, the complex and one equivalent of the bridging ligand (the excess of 0.5 equivalents ligand are being considered soluble, see footnote in **Table 3**) and dividing it by the total weight of the sample. As a result, the weight fraction of the insoluble part increases to 82% (**Table 3**). This indicates that the fraction of less soluble or insoluble parts needs to be around 80 % or higher for the formation of rods or worm-like structures.

Table 3. Model calculations on the P4VP/SCO nanocomposite core fraction (insoluble parts) for sample **5e**.

Insoluble parts			Whole sample		
Fraction	Calculation	Weight [mg]	Fraction	Calculation	Weight [mg]
P4VP	50 mg 61 wt%	30.5	dBCP	50 mg 100 wt%	50
Complex [FeL][a)]	5·29 mg ·0.86	124.7	Complex [FeL][a)]	0.86·5·29 mg	124.7
Ligand bipy[b)]	5·15.2 mg /1.5	50.7	Ligand bipy[b)]	5·15.2 mg	76
Total		205.9	Total		250.7

a) MeOH replaced by 4,4'-bipyridine during the synthesis and therefore considered as a solvent which is removed after the reaction, leading to the factor 0.86; b) only 1 equivalent bipy is involved in the formation of the CP, the excess is regarded soluble.

In literature, for similar examples the molecular weights used are significantly lower, ranging from 20 000 g mol^{-1} to 70 000 g mol^{-1} with varying P4VP content, usually accompanied by the formation of spheres.[57–62] So far there are only few cases known, where the introduction of organic or inorganic material into the dBCPs triggered the formation of rods.[61,62] One example are PB-*b*-P2VP dBCPs, where the formation of worm-like micelles is observed for a core fraction of 80% and more.[64] This highlights the impact of the size of the P4VP core on the stabilization of spherical nanocomposite particles and the design principles that can be followed.

MAGNETIC PROPERTIES

The samples **1-5,c-d** were studied at room temperature by ^{57}Fe Mössbauer spectroscopy, and sample **5e** was additionally analyzed by temperature-dependent measurements between 80 K and 300 K. As a local nuclear probe technique, Mössbauer spectroscopy offers a deeper insight on the oxidation and spin states of the iron centers and by this supports the interpretation of the magnetic measurements of composite materials, where the diamagnetic polymer matrix needs to be considered. With the exception of the as-synthesized sample **5e** (see below), the room temperature Mössbauer spectra of all investigated compounds show only one distinct doublet with an isomer shift of δ = 0.93 mm s^{-1} – 0.96 mm s^{-1} and a quadrupole splitting of ΔE_Q = 2.15 mm s^{-1} – 2.20 mm s^{-1} that clearly corresponds to a Fe(II) HS species.[67] The spectra of all samples are presented in **Figures S18**-**S22** and **Figure S29** along with the determined isomer shift δ, the quadrupole splitting ΔE_Q and the line width Γ (**Table S1** and **Table S3**).

Magnetic susceptibility measurements were performed on samples **1-5,c-e** with a SQUID magnetometer. The SCO properties (hysteresis width, transition temperature, and HS fraction) of the as-synthesized product can be altered by thermal annealing. This effect occurs due to the recrystallization of the CP inside the polymeric micelles at annealing temperatures above the glass transition temperature T_g of PS (109 °C/382 K, see **Figure S3**), proven by temperature-dependent powder X-ray diffraction (*T*-PXRD).[17]

To investigate the impact of thermal annealing on the different samples, several cooling and heating cycles were made for each sample where the maximum temperature was increased step-wise from 300 K to 370 K, 380 K and 400 K. All measurements were made in the sweep mode with a velocity of 5 K min^{-1}. After thermal annealing of the samples at 400 K for 1 h, the final measurement was made first in the sweep mode (5 K min^{-1}) and then in the settle mode (before each measurement point the temperature was allowed to stabilize, average measurement velocity 0.5 K min^{-1}) to allow the investigation of kinetic effects.[68,69] As representatives, the magnetic properties of the smallest and the largest nanoparticles with five synthesis cycles, **1e** and **5e**, are displayed as $\chi_M T$ vs. *T* plots in **Figure 5A** and **B** in the temperature range between 300 K and 50 K, to illustrate the differences in the annealing behavior as a function of the particle size and shape. The full temperature range of all samples with all measurement cycles is given in the Supporting Information, **Figures S23**-**S27**. Moreover, the residual HS fraction was calculated from the measurements by dividing the $\chi_M T$ value at 50 K by the starting value at 300 K (**Table S2**). In line with the results from Mössbauer spectroscopy, all samples are predominantly in the iron(II) HS state at room temperature with $\chi_M T$ values between 3.2 cm^3 K mol^{-1} and 3.3 cm^3 K mol^{-1}. For the as-synthesized samples (black curve in **Figure 5** and in the SI), the $\chi_M T$ values at 50 K are surprisingly very similar between 1.8 cm^3 K mol^{-1} and 1.6 cm^3 K mol^{-1}, thus approximately 50% of the iron centers are involved in the SCO (γ_{HS} = 0.5), independent of the particle size, complex loading and synthesis conditions (excess of bipy). With increasing particle size (samples **1** to **5**) and improved synthesis conditions (**c**, **d** to **e**) the curve progression is slightly more abrupt, but apparently it does not influence the completeness of the spin crossover.

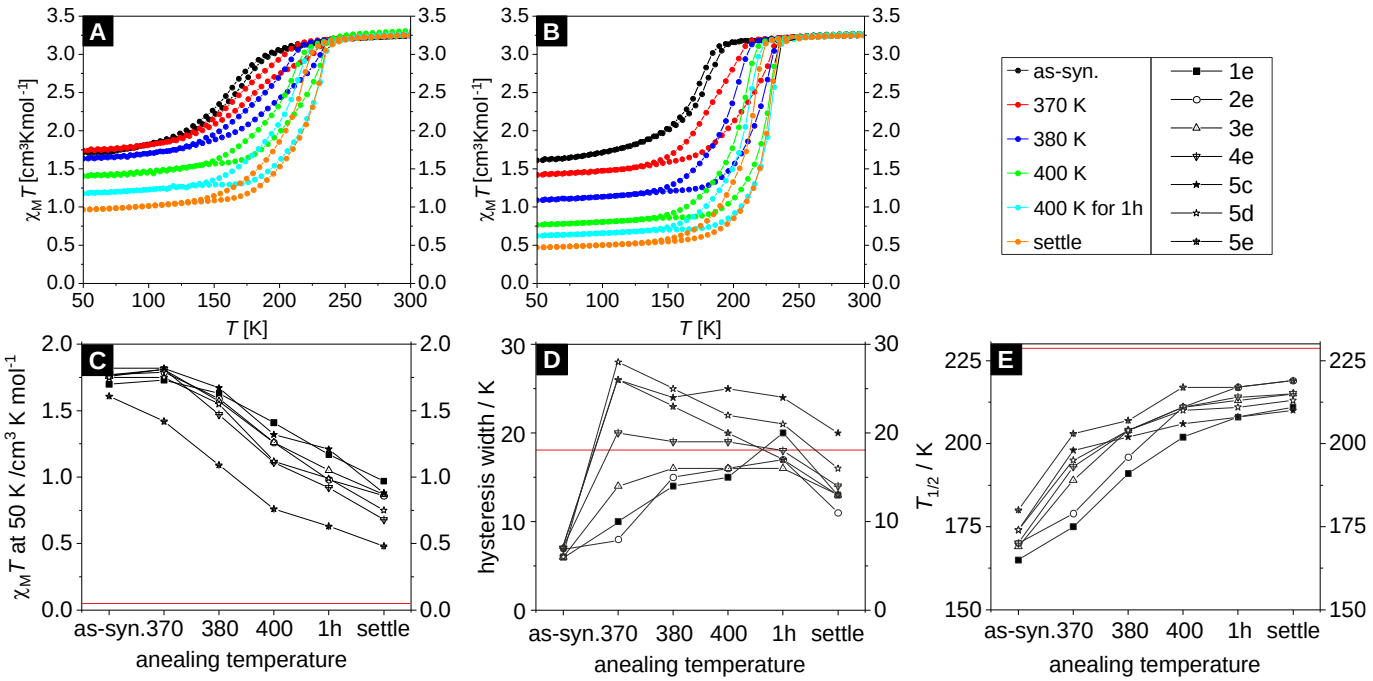

Figure 5. TOP: Comparison of the magnetic susceptibility measurements in the temperature range from 50 K to 300 K for the samples **1e** (A) and **5e** (B) in sweep mode (black, red, blue, green and turquoise) and settle mode (orange). Detailed information about the impact on the cooling and heating cycles on the SCO properties are noted in **Table S2.** The measurements for all samples in the complete temperature range from 50 K to 400 K with all measurement cycles is given in **Figures S23**-**S27**. BOTTOM: Impact of particle size (used dBCP, samples 1-5) and composition (cycle count, stoichiometry, samples c, d and e) on the SCO parameters before and after thermal treatment for selected samples. (C) HS fraction given as $\chi_M T$ value at 50 K, (D) hysteresis width at $T_{1/2}$ in K and (E) average transition temperature $T_{1/2}$. The red line illustrates the expected values for the bulk material ($\chi_M T$ = 0.05 cm³Kmol⁻¹, 18 K hysteresis width, average $T_{1/2}$ = 227 K)

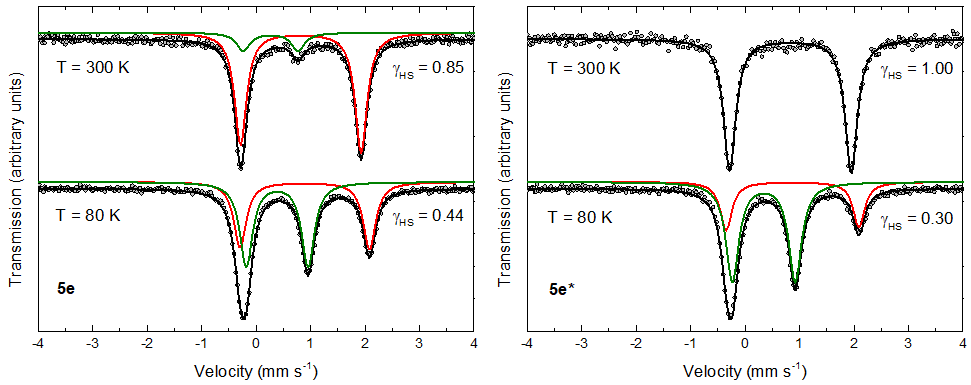

Figure 6. Zero-field ^{57}Fe Mössbauer spectra of compounds **5e** (as-synthesized, left panel) and **5e*** (after thermal annealing at 393 K for 3 h under nitrogen atmosphere, right panel), recorded at 300 K and 80 K. Symbols: Experimental data. Lines: The spectra were analyzed with one or two doublets of Lorentzian lines, respectively. The colored lines represents the individual sub-spectra of the fit, which are attributed to Fe(II) low-spin (green) and Fe(II) high-spin sites (red, see text). The parameters of the fits are summarized in **Table S3**.

The changes in the SCO properties are more pronounced for the fully annealed samples (orange curve in **Figure 5**). Here, we can show that the enlargement of the particles and the morphological changes into worm-like structures alters the SCO to be more complete, e.g. with HS fractions at 50 K changing from γ_{HS} = 0.3 for sample **1e** to γ_{HS} = 0.14 for sample **5e**. In addition, the optimization of the synthesis by reducing the amount of bridging ligand bipy improves the completeness of the SCO in the CP-dBCP nanocomposites, as indicated by the residual HS fraction with γ_{HS} = 0.23 vs. γ_{HS} = 0.14 for samples **5d** and **5e**, respectively. This correlation is illustrated

graphically in **Figure 5C**, where the $\chi_M T$ values at 50 K are plotted vs. the annealing temperature for selected samples. Apparently, for the as-synthesized samples the CP chain length in the NPs is independent from the particle size, leading similar γ_{HS} values both, at room temperature and at 50 K. This indicates that for the as-synthesized samples the CP chain length and by this γ_{HS} only depends on the synthesis cycles, which were not varied here. Upon confined recrystallization of the CP within the polymer shell, the chain lengths increase and now the γ_{HS} values at 50 K correlate with the particle size and loading. *T*-PXRD pattern were measured for the samples **1-5e** to confirm the recrystallization of the CP. The relative intensity of the newly detected reflexes after thermal annealing increased continuously from sample **1e** to **5e** (**Figure S28**), in line with the increase of the particle size.

The difference in particle size, crystallinity, but also the used synthesis conditions do influence the transition temperature $T_{1/2}$ and the hysteresis width of the samples, two further relevant spin crossover properties which need to be discussed to evaluate the application potential of the nanocomposites. Both parameters change upon thermal treatment, but the progression of those changes strongly depends on the particle size and composition (see **Figures 5D,E**, **Table S2**). Again, for the as-synthesized samples the hysteresis width and transition temperature are very similar. Upon annealing, for all samples a similar shift of the transition temperature to higher temperatures is observed (**Figure 5E**), independent of particle size, complex loading and bipy excess. In contrast to this, a significant impact of those three parameters on the change in hysteresis width upon thermal treatment is observed (**Figure 5D**). Please note the almost identical thermal hysteresis width for all as-synthesized samples. For the larger particles of samples **5c-e**, both the hysteresis width and the completeness of the SCO significantly improved already after the first heating cycle. Indeed, the thermal hysteresis loop is wider than for the corresponding bulk material (27 K in the composite nanoparticles vs. 18 K for the bulk). In contrast to this, for the smallest particles (samples **1e**, **2e**) the HS fraction did not change significantly for the first two annealing cycles and the hysteresis is slowly increasing with each cycle. In the settle mode, the final hysteresis widths of the samples **1-5e** are smaller compared to the sweep mode and furthermore they all are in the same order of magnitude (see **Table S2** and **Figure 5D**). This indicates that the pronounced differences observed in the sweep mode during the annealing are kinetic effects imposed by the polymer matrix, which are more pronounced for the smaller particles and lower complex loading. For the smaller particles the PS matrix is more rigid due to the higher overall PS fraction leading to a more pronounced influence on the SCO properties. Interestingly, for the largest particles **5c** and **5d**, where a higher bipy excess was used during the synthesis, significantly wider thermal hysteresis loops are observed also in the settle mode (**Figure 5D**). Thus both parameters, the used dBCP and the synthesis conditions can be used to fine-tune the SCO properties of the nanocomposite.

Zero-field, temperature-dependent ^{57}Fe Mössbauer spectra were recorded for the as-synthesized sample **5e** and for the annealed sample **5e*** between 80 K and 300 K in the cooling and heating mode to follow the spin crossover and to confirm the changes observed in the magnetic measurements upon annealing. Selected spectra are given in **Figure 6**. Further temperature-dependent Mössbauer spectra and the summary of the Mössbauer parameters obtained from the fits are given in **Figure S29** and **Table S3**. The as-synthesized sample shows two doublets at 300 K, where the majority species (85%) represents an iron(II) HS species corresponding to the formed iron(II) CP $[FeL(bipy)]_n$ inside the dBCP.[67] The minority species shows characteristic Mössbauer parameters (δ = 0.39 mm s^{-1}, ΔE_Q = 1.01 mm s^{-1}) for an iron(II) LS species, which was detected before and can be assigned to the iron(II) complex [FeL] coordinated to two vinyl pyridine units of the coordination polymer, i.e. $[FeL(VP)_2]$.[52] Upon cooling of the sample in the spectrometer, the area of the doublet corresponding to the iron(II) LS species increased and the residual iron(II) HS fraction was lowered to 44% at 80 K, which is in good agreement with the residual HS fraction of the magnetic measurement of 51% at 80 K. After thermal annealing, the measurement procedure was repeated. Interestingly, for the annealed sample **5e*** the iron(II) LS species $[FeL(VP)_2]$ disappeared due to the re-crystallization of the coordination polymer and only one iron(II) HS doublet is observed at 300 K. Thus the Mössbauer spectra confirm the changes observed in the magnetic measurements and the *T*-dependent PXRD patterns. Upon cooling below 215 K (in the spin crossover region), the iron(II) HS fraction of the annealed sample is constantly lower than for the as-synthesized sample **5e** at the same temperature. At 80 K, the iron(II) HS fraction of sample **5e*** was decreased to 30%. In **Table S4**, the γ_{HS} values of **5e** and **5e*** obtained by magnetic susceptibility measurements and Mössbauer spectroscopy are compared. The systematically lower γ_{HS} values of the annealed sample obtained by SQUID magnetometry can be explained by the different annealing environments for the two measurements (see SI).

SEM was additionally performed on the samples **1-5e** to analyze the surface of the nanocomposites. The surface was found to be crystal-free for the five samples before thermal annealing, indicating the successful incorporation and confinement of the CP into the polymeric micelles (**Figures S30**-**S34**). After annealing, some of the samples appeared to have crystalline parts in the SEM images. While the surface of the annealed samples **1e*** and **2e*** remained crystal-free, crystals were observed for the samples **3e***, **4e***, and **5e***. Interestingly, the presence of crystals on the surface of sample **5e*** is less prominent than for the other two samples, which may be an effect of

an improved formation of the CP inside the elongated worm-like micelles. To understand the origin of those crystalline parts and to rule out agglomeration and the growth of CP microcrystals outside the polymeric micelles, the nanocomposites were analyzed again by TEM and DLS after annealing. The average hydrodynamic diameters D_h of the re-dispersed samples range from 106 nm ± 67 nm (**1e***) to 246 nm ± 149 nm (**5e***) (**Figure S35**). Particle core sizes and core widths D_{core} of the annealed products are 14 nm ± 2 nm (**1e***) to 65 nm ± 5 nm (**5e***) (**Figure S36**). In **Table S5**, the comparison of the core size/core width and the hydrodynamic diameter of the as-synthesized and the annealed samples is given, showing that very similar results are obtained. Please note that the magnetic properties of samples containing CP SCO microcrystals differ strongly from those of the samples reported here (i.e. bulk-like behavior of as-synthesized samples, see **Figure S37**). This indicates that the crystals found in the SEM measurements are not the bulk iron(II) complex, but of different origin. As illustrated in the SI, (Figures S38 and S39), the crystals are presumably 4,4'-bipyridine which was used in excess during the synthesis.

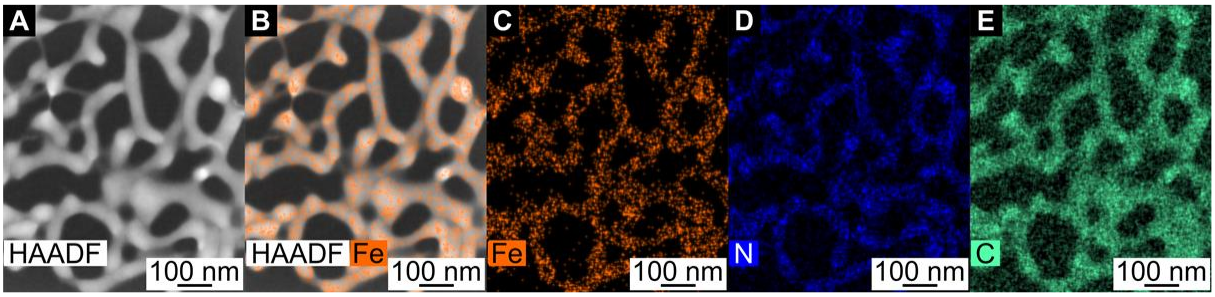

Figure 7. HAADF image of sample **5d** showing the worm-like structures (A), an overlay of the iron signal received from TEM-EDX measurements and the HAADF image (B), and the individual images of the iron (C), nitrogen (D), and carbon (E) signals from TEM-EDX.

SURFACE PROPERTIES AND COMPOSITION OF 5D

Transmission electron microscopy – energy dispersive X-ray (TEM-EDX) measurements were additionally performed on the sample **5d** with the widest thermal hysteresis loop to evaluate the spatial distribution of iron inside the SCO CP-dBCP nanocomposite. It was expected that the iron can only be detected inside the polymeric structure. **Figure 7** shows the high-angle annular dark field (HAADF) image of sample **5d** (A) and the respective overlay of the HAADF image with the iron signal from TEM EDX (B). The images of the distribution of only iron (C), nitrogen (D), and carbon (E) are presented as well. Iron was only detected inside the SCO CP-dBCP nanocomposite and is homogenously distributed throughout the polymer structure. Image C (**Figure 7**) shows that the spatial distribution of the iron signal is identical to that of the signals of nitrogen and carbon of the dBCP. Two energy spectra were calculated by the integration of two different areas (but identical in size) of the sample. One spectrum was taken on the area of the SCO CP-dBCP nanocomposite and the other one outside (**Figure S40**). The results confirm that iron was only found inside the SCO CP-dBCP nanocomposite, indicating a regio-selective incorporation of the SCO CP into the dBCP micelles.

As the worm-like structures indicated that there might be an impact on the sample surface, BET measurements using krypton gas were performed for the nanocomposite **5d** and the corresponding bulk material for comparison at 77 K. Before measurement, the samples were heated to 100 °C under vacuum for 6 h. With 5.5 $m^2\ g^{-1}$ for the bulk and 4.0 $m^2\ g^{-1}$ for the composite, similar values were obtained. Thus the structures in **Figure 7** and **Figure 4d** are only 2D structures and no additional porosity is introduced yet. This challenge will be addressed in future research.

Experimental

Materials and methods.

All SCO CP-dBCP syntheses were performed under inert conditions using argon 5.0 (purity ≥ 99.999%) using Schlenk tube technique and repeated at least twice. Tetrahydrofuran (THF, p.a. grade) for the SCO syntheses was obtained from Bernd Kraft and degassed with argon for at least 30 min. [FeL(MeOH)$_2$] was synthesized as described before.[70] 4,4´-bipyridine (98%) was obtained from Alfa Aesar and used as received.

THF (Fischer Scientific, ≥ 99.8%) for anionic polymerization was purified by successive distillation over calcium hydride (CaH_2, Merck) and potassium (K, Sigma-Aldrich) under N_2 atmosphere. Styrene (S, Sigma-Aldrich, > 99%)

was purified over dibutyl magnesium (Bu_2Mg, Sigma-Aldrich, 1M in heptane) and 4-vinylpyridine (4VP, Acros Organics, 95%) over triethyl aluminum (Et_3Al, Sigma-Aldrich, 1M in heptane), respectively, followed by condensing into storage ampoules. 1,1-Diphenylethylene (DPE, Acros Organics, 98%) was purified by addition of *sec*-butyllithium (*sec*-BuLi, Acros Organics, 1.3M in cyclohexane/hexane 92/8 v/v) and subsequent distillation.

Gel permeation chromatography (GPC) was performed employing *N,N*-dimethylformamide (DMF) with lithium bromide (5 g L^{-1}) as eluent and GRAM columns (300 x 8 mm, 10 µm particle size, PSS Mainz) with 100 and 3000 Å pore sizes. The samples were measured on a SEC 1260 Infinity system (Agilent Technologies) at a flow rate of 0.5 mL min^{-1} at 23 °C, using a refractive index detector (Agilent Technologies). The calibration was done with narrowly distributed polystyrene standards (PSS calibration kit) and toluene (HPLC grade) was used as internal standard.

MALDI-ToF MS was performed on a Bruker Autoflex maX instrument equipped with a 355 nm solid-state laser in the reflectron and linear mode and 20 kV acceleration voltage. The samples were prepared according to the dried droplet method. Therefore, matrix (trans-2-[3-(4-tert-butylphenyl)-2-methyl-2-propenylidene]malononitrile (DCTB), 10 g L^{-1} in THF), analyte (10 g L^{-1} in THF) and salt (silver trifluoroacetate, 10 g L^{-1}) were dissolved and mixed in the ratio of 20 : 5 : 1 and 0.5 µL of the mixture was placed and dried on the target plate.

1H-nuclear magnetic resonance (NMR) spectra were acquired with a Bruker Ultrashield 300 spectrometer using $CDCl_3$ as solvent.

The differential scanning calorimetry (DSC) measurements were performed on a Phoenix 204 F1 (Netzsch) under nitrogen atmosphere, using aluminum crucibles (temperature range: 20 – 200 °C, scanning rate: 10 K min^{-1}).

Infrared (IR) spectra were collected from a Perkin Elmer Spectrum 100 FT-IR (ATR). The samples were measured directly as solids.

For elemental analysis, the carbon, nitrogen, and hydrogen contents were determined with a Vario EL III (Elementar Analysensysteme GmbH) with acetanilide as standard or at a Unicube (Elementar Analysensysteme GmbH) with sulfanilamide as standard. The samples were placed in tin boats and measured at least twice. The average of the measurements was used.

Magnetic susceptibility measurements were performed at a Quantum Design MPMS-XL-5 SQUID magnetometer. A field strength of 3 T was applied and a temperature range of 50 – 400 K was used to determine the temperature dependency of the magnetism and the spin crossover behavior. Sweep mode was used for the five cycles with a cooling and heating rate of 5 K min^{-1}. The final measurement was performed in settle mode with an average cooling and heating rate of 0.5 K min^{-1} between 50 K and 300 K. The samples were prepared in gelatin capsules placed in a plastic straw. The measured values were corrected for the diamagnetism of the sample holder, the polymer matrix (measured values) and the ligand (tabulated Pascal constants).

The room-temperature zero-field 57Fe Mössbauer spectra were recorded in transmission geometry with constant acceleration using a conventional Mössbauer spectrometer with a 50 mCi ^{57}Co(Rh) source. The samples were sealed in the sample holder in an argon atmosphere. The spectra were fitted using Recoil 1.05 Mössbauer Analysis Software.[71] The isomer shift values are given with respect to a α-Fe reference at room temperature.

The temperature-dependent zero-field 57Fe Mössbauer measurements on powders of **5e** and **5e*** (79.5 mg) were carried out with a standard WissEl and Halder transmission spectrometer and sinusoidal velocity sweep. The measurements between 80 K and 300 K were conducted on a CryoVac continuous-flow cryostat with He or N_2 contact gas. After positioning the sample container (made of Teflon or PEEK), the sample chamber was evacuated, flushed six times with He or N_2 gas, and kept at ca. 50 - 100 mbar during the measurement. The temperature was measured with a calibrated silicon diode located close to the sample container, providing a temperature stability of better than ± 0.1 K. The nominal activity of the ^{57}Fe Mössbauer source was 50 mCi of ^{57}Co in a rhodium matrix, which was stored at ambient temperatures during the measurements. Velocity calibration was done with an α-Fe foil at 300 K; the minimum experimental line width (FWHM) was < 0.24 mm s^{-1}. Isomer shifts (δ) were specified relative to metallic Fe at ambient temperature but were not corrected in terms of the second-order Doppler shift. The spectra were analyzed by least-square fits using doublets of Lorentzian lines utilizing the software package NORMOS.[72]

Scanning electron microscopy (SEM) micrographs were taken on a Zeiss LEO 1530 GEMINI and a Zeiss Ultra plus. The acceleration voltage was set to 3 kV (with a Schottky-field-emission gun) using an in-lens secondary electron detector. The sample was sputter-coated with a 1.3 nm platinum layer.

Room temperature powder X-ray diffraction (PXRD) data were collected with a STOE StadiP X-Ray diffractometer in transmission geometry between 2Θ = 5° and 30° for all samples, which were placed on flat surfaces. Cu-$K_{\alpha 1}$ radiation (λ = 1.541 Å) was used for the measurements together with a Mythen 1K detector. Temperature-dependent powder X-ray diffraction (*T*-PXRD) patterns were recorded using a Bragg-Brentano type diffractometer (X'PERT-Pro, PANalytical with Cu-$K_{\alpha 1}$ radiation (λ = 1.541 Å), equipped with a secondary monochromator to suppress fluorescence. The sample was placed on a flat surface in a flowing nitrogen atmosphere in an XRK chamber during the measurement.

Transmission electron microscopy (TEM) was taken at a Zeiss CEM902 electron microscope (Zeiss, Oberkochen, Germany) and a JEOL JEM-2200FS electron microscope. Samples were dissolved in THF. The solution was dropped on a carbon coated copper grid (mesh 200, Science Services, Munich). Electron acceleration voltage was set to 80 kV (CEM902) and 200 kV (JEOL 2200FS). For the Zeiss CEM902 micrographs were taken with a MegaView III / iTEM image acquiring and processing system from Olympus Soft Imaging Systems (OSIS, Münster, Germany) and an Orius 830 SC200W / DigitalMicrograph GMS 2.3 system from Gatan (Munich, Germany). For the JEOL JEM-2200FS micrographs were taken with an OneView 1095 / DigitalMicrograph GMS 3.2 system from Gatan (Munich, Germany). Both microscopes are Energy-Filtering TEMs (EFTEM). All micrographs were acquired in near focus bright field mode and zero-loss filtered. For the Zeiss CEM902 an objective aperture of 60µm and in case of the JEOL JEM-2200FS an objective aperture of 120µm were used. Particles size measurements were done with "ImageJ" image processing software developed by Wayne Rasband (National Institutes of Health, USA).

For cryo-TEM studies, a sample droplet of 2 µL was put on a lacey carbon filmed copper grid (Science Services, Munich, Germany). Subsequently, most of the liquid was removed with blotting paper leaving a thin film stretched over the lace holes. The specimens were instantly shock frozen by rapid immersion into liquid nitrogen in a temperature-controlled freezing unit (Zeiss Cryobox, Carl Zeiss Microscopy GmbH, Jena, Germany). The temperature was monitored and kept constant in the chamber during all the sample preparation steps. The specimen was inserted into a cryotransfer holder (CT3500, Gatan, Munich, Germany) and transferred to a Zeiss / LEO EM922 Omega EFTEM (Zeiss Microscopy GmbH, Jena, Germany). Examinations were carried out at temperatures around 90 K. The TEM was operated at an acceleration voltage of 200 kV. Zero-loss filtered images (□E = 0 eV) were taken under reduced dose conditions (100 – 1000 e nm^{-2}). All images were registered digitally by a bottom mounted CCD camera system (Ultrascan 1000, Gatan, Munich, Germany) combined and processed with a digital imaging processing system (Digital Micrograph GMS 1.9, Gatan, Munich, Germany).

Dynamic light scattering (DLS) measurements were done at an Anton Paar Litesizer 500 in quartz glass cuvettes from Hellma at 25 °C in backscattering mode (175°). One measurement consists of six consecutive runs. Samples were dispersed in THF at a concentration of 2 g L^{-1}. The unfiltered solutions were used. A cumulant fit was used for fitting the experimental data

Synthetic procedures.

Synthesis of the PS-b-P4VP diblock copolymers: The PS-*b*-P4VP diblock copolymers were synthesized by sequential living anionic polymerization in THF using a laboratory autoclave (1 L, Büchi AG). Styrene was polymerized first for 30 min using *sec*-BuLi as initiator at -80 °C. After complete conversion of styrene, a sample was taken for GPC and MALDI-ToF analyses. Subsequently, 1,1-diphenylethylene was added to the living polystyryllithium (equimolar amount to initiator), followed by the addition of 4-vinylpyridine (4VP). After 4 h the polymerization was terminated with degassed methanol followed by precipitation in deionized water to isolate the diblock copolymer. The average molecular weights of the PS-*b*-P4VP diblock copolymers were determined from ^{1}H-NMR ($CDCl_3$), utilizing the absolute molecular weight of the PS precursor obtained by MALDI-ToF MS for signal calibration. As the solubility of the P4VP block in THF strongly decreases with its chain length[73], micellization and, thus, a significant increase in solution viscosity occurred during the synthesis of the diblock copolymers with high P4VP fractions. Nevertheless, polymerization of 4VP proceeds within the core of the formed micelles to yield the desired diblock copolymers. However, this resulted in an increase in dispersity with increasing P4VP weight fraction (**Table 1**). The diblock copolymer $S_{39}V_{61}^{162}$ was additionally purified by extraction with cyclohexane/THF (1/1 v/v) over night to remove a small fraction of PS homopolymer formed by termination upon addition of 4VP.

Synthesis of the SCO CP-dBCP nanocomposite particles in SV-15: 50 mg $S_{85}V_{15}^{154}$ and 6.7 mg (15 µmol) [FeL(MeOH)$_2$] were dissolved in 20 mL THF in a 50 mL Schlenk flask. The solution was refluxed for 2 h. After cooling, 5.9 mg (37.5 µmol, 2.5 eq) 4,4'-bipyridine were added and the solution refluxed again for 1 h. After a short cool down to RT, 6.7 mg (15 µmol) [FeL(MeOH)$_2$] and 5.9 mg (37.5 µmol, 2.5 eq) 4,4'bipyridine were added simultaneously and the solution was refluxed again for 1 h. The simultaneous addition of the reactants and the subsequent reflux of the solution were repeated up to three more times (samples **1a** to **1d**). Consecutively, the solvent was removed by cold distillation and the resulting dark brown polymeric solid was dried *in vacuo*. For sample **1e** the amount of 4,4'-bipyridine for each cycle was reduced to 3.5 mg (22.5 µmol, 1.5 Eq).

1a: Anal. found (%): C 72.16, H 7.40, N 2.65; **1b**: Anal. found (%): C 57.90, H 6.83, N 3.37; **1c**: Anal. found (%): C 66.14, H 6.81, N 5.10; **1d**: Anal. found (%): C 67.06, H 6.59, N 5.85; **1e**: Anal. found (%): C 64.27, H 6.43, N 4.70.

Synthesis of the SCO CP-dBCP nanocomposite particles in SV-21: 50 mg $S_{79}V_{21}^{119}$ and 9.4 mg (21 µmol) [FeL(MeOH)$_2$] were dissolved in 20 mL THF in a 50 mL Schlenk flask. The solution was refluxed for 2 h. After cooling, 8.2 mg (52.5 µmol, 2.5 eq) 4,4'-bipyridine were added and the solution refluxed again for 1 h. After a short cool down to RT, 9.4 mg (21 µmol) [FeL(MeOH)$_2$] and 8.2 mg (52.5 µmol, 2.5 eq) 4,4'bipyridine were added simultaneously and the solution was refluxed again for 1 h. The simultaneous addition of the reactants and the subsequent reflux of the solution were repeated three more times (samples **2a** to **2d**). Consecutively, the solvent was removed by cold distillation and the resulting dark brown polymeric solid was dried *in vacuo*. For sample **2e** the amount of 4,4'-bipyridine for each cycle was reduced to 4.9 mg (31.5 µmol, 1.5 Eq).

2a: Anal. found (%): C 71.85, H 6.33, N 4.11; **2b**: Anal. found (%): C 68.00, H 6.80, N 6.20; **2c**: Anal. found (%): C 66.92, H 6.64, N 6.61; **2d**: Anal. found (%): C 68.88, H 5.77, N 7.52; **2e**: Anal. found (%): C 62.13, H 6.21, N 5.77.

Synthesis of the SCO CP-dBCP nanocomposite particles in SV-35: 50 mg $S_{65}V_{35}^{131}$ and 14.8 mg (33 µmol) [FeL(MeOH)$_2$] were dissolved in 20 mL THF in a 50 mL Schlenk flask. The solution was refluxed for 2 h. After cooling, 12.9 mg (82.5 µmol, 2.5 eq) 4,4'-bipyridine were added and the solution refluxed again for 1 h. After a short cool down to RT, 14.8 mg (33 µmol) [FeL(MeOH)$_2$] and 12.9 mg (82.5 µmol, 2.5 eq) 4,4'bipyridine were added simultaneously and the solution was refluxed again for 1 h. The simultaneous addition of the reactants and the subsequent reflux of the solution were repeated three more times (samples **3a** to **3d**). Consecutively, the solvent was removed by cold distillation and the resulting dark brown polymeric solid was dried *in vacuo*. For sample **3e** the amount of 4,4'-bipyridine for each cycle was reduced to 7.8 mg (50 µmol, 1.5 Eq).

3a: Anal. found (%): C 68.70, H 7.12, N 5.36; **3b**: Anal. found (%): C 64.67, H 6.15, N 6.88; **3c**: Anal. found (%): C 63.66, H 6.56, N 7.18; **3d**: Anal. found (%): C 66.60, H 6.27, N 8.29; **3e**: Anal. found (%): C 60.99, H 5.96, N 6.88.

Synthesis of the SCO CP-dBCP nanocomposite particles in SV-42: 50 mg $S_{58}V_{42}^{157}$ and 17.9 mg (40 µmol) [FeL(MeOH)$_2$] were dissolved in 20 mL THF in a 50 mL Schlenk flask. The solution was refluxed for 2 h. After cooling, 15.6 mg (100 µmol, 2.5 eq) 4,4'-bipyridine were added and the solution refluxed again for 1 h. After a short cool down to RT, 17.9 mg (40 µmol) [FeL(MeOH)$_2$] and 15.6 mg (100 µmol, 2.5 eq) 4,4'bipyridine were added simultaneously and the solution was refluxed again for 1 h. The simultaneous addition of the reactants and the subsequent reflux of the solution were repeated three more times (samples **4a** – **4d**). Consecutively, the solvent was removed by cold distillation and the resulting dark brown polymeric solid was dried *in vacuo*. For sample **4e** the amount of 4,4'-bipyridine for each cycle was reduced to 9.4 mg (60 µmol, 1.5 Eq).

4a: Anal. found (%): C 66.51, H 6.63, N 5.63; **4b**: Anal. found (%): C 69.14, H 5.74, N 8.67; **4c**: Anal. found (%): C 64.83, H 6.35, N 8.22; **4d**: Anal. found (%): C 66.19, H 6.20, N 9.04;

4e: Anal. found (%): C 61.64, H 5.85, N 7.63.

Synthesis of the SCO CP-dBCP nanocomposite particles in SV-61: 50 mg $S_{39}V_{61}^{162}$ and 29 mg (65 µmol) [FeL(MeOH)$_2$] were dissolved in 20 mL THF in a 50 mL Schlenk flask. The solution was refluxed for 2 h. After cooling, 25.4 mg (162.5 µmol, 2.5 eq) 4,4'-bipyridine were added and the solution refluxed again for 1 h. After a short cool down to RT, 29 mg (65 µmol) [FeL(MeOH)$_2$] and 25.4 mg (162.5 µmol, 2.5 eq) 4,4'bipyridine were added simultaneously and the solution was refluxed again for 1 h. The simultaneous addition of the reactants and the subsequent reflux of the solution were repeated three more times (samples **5a** – **5d**). Consecutively, the solvent was removed by cold distillation and the resulting dark brown polymeric solid was dried *in vacuo*. For sample **6e** the amount of 4,4'-bipyridine for each cycle was reduced to 15.2 mg (97.5 µmol, 1.5 Eq).

5a: Anal. found (%): C 69.01, H 6.14, N 9.11; **5b**: Anal. found (%): C 64.66, H 5.46, N 9.68; **5c**: Anal. found (%): C 65.97, H 5.50, N 10.49; **5d**: Anal. found (%): C 66.22, H 5.70, N 10.64; **5e**: Anal. found (%): C 62.60, H 5.62, N 8.93.

Conclusions

Five different dBCPs with a varying P4VP content (SV-15 to SV-61) have been prepared. The TEM and cryo-TEM images of the neat dBCPs showed spherical micelles with core diameters D_{core} of 15 nm ± 2 nm (SV-15) to 73 nm ± 9 nm (SV-61) and D_{cryo} of 26 nm ± 2 nm (SV-15) to 71 nm ± 4 nm (SV-61). These polymers were utilized as nanoreactors in the synthesis of iron(II)-based CP NPs with well-defined size, shape and SCO properties. The nanocomposite particles based on the dBCPs SV-15 to SV-42 were also spherical and the size was similar to the neat dBCP micelles, underlining the templating effect of the dBCPs. Interestingly, the morphology of the nanocomposite particles changed to worm-like structures for the nanocomposite particles synthesized with SV-61 and the particle core widths were determined by TEM (D_{core} = 60 nm ± 8 nm) and cryo-TEM (D_{cryo} = 84 nm ± 10 nm), respectively. These results indicate that the introduction of the CP induced a morphological change by increasing the fraction of the insoluble parts (P4VP cores with incorporated CP) of the nanocomposite particle. Additionally, it was shown that the magnetic properties of the SCO CP-dBCP nanocomposites can be altered by several factors to approximate a bulk-like behavior: (1) The reduction of the amount of the bridging ligand bipy from 2.5 eq to 1.5 eq. This resulted in a lower residual HS fraction γ_{HS} in all samples. (2) The enlargement of the spherical particle cores from 14 nm to 58 nm also resulted in a decrease of γ_{HS} from 30 % (**1e**) to 21 % (**4e**). (3) The thermal annealing of the SCO CP-dBCP composites led to a shift in the transition temperature and, again, in a decrease of γ_{HS}. (4) The change of the morphology of the nanocomposite particles to worm-like structures allowed the CP to crystallize in longer strands. As a result, the γ_{HS} value ultimately reached 14% (**5e***). Furthermore, for some of the nanocomposites thermal hysteresis loops are observed that are wider than those of the bulk material. In addition, TEM EDX of a nanocomposite containing worm-like structures (**5d**) proved that the iron containing SCO CP is only located inside the polymeric structure and no iron can be detected outside of the micelles. Thus, with the presented approach both, size and morphology, of coordination polymers and networks can be tailored in a well-defined way. This concept can be transferred to a wide range of coordination compounds with different functionalities. Furthermore, the obtained structures are stable both in the solid state and in solution, opening ways different types of processing for application, for example as sensor material.

Acknowledgements

Financial support of the University of Bayreuth and the SFB 840 (TP A10 and A2) is gratefully acknowledged. Christoph Göbel was supported by the BayNAT program of the University of Bayreuth. We thank Dr. Jana Timm and Prof. Dr. Roland Marschall (Physical Chemistry III, Universität Bayreuth) for BET measurements, Florian Puchtler (Inorganic Chemistry I, Universität Bayreuth) for room temperature PXRD, Dr. Christine Denner (Inorganic Chemistry II, Universität Bayreuth) for SEM measurements and Rika Schneider (Macromolecular Chemistry II, Universität Bayreuth) for DSC, GPC, and NMR measurements of the dBCPs. DB thanks Prof. Dr. F. J. Litterst (Institut für Physik der Kondensierten Materie) at TU Braunschweig for providing access to the ^{57}Fe Mössbauer spectrometer.

Notes and references

1 Q. Zhang, E. Uchaker, S. L. Candelaria and G. Cao, Nanomaterials for energy conversion and storage, Chem. Soc. Rev., 2013, **42**, 3127–3171.

2 E. Roduner, Size matters: why nanomaterials are different, Chem. Soc. Rev., 2006, **35**, 583–592.

3 P. Liu, J. R. Williams and J. J. Cha, Topological nanomaterials, Nat. Rev. Mater., 2019, **4**, 479–496.

4 C. L. Nehl and J. H. Hafner, Shape-dependent plasmon resonances of gold nanoparticles, J. Mater. Chem., 2008, **18**, 2415.

5 R. Himstedt, P. Rusch, D. Hinrichs, T. Kodanek, J. Lauth, S. Kinge, L. D. A. Siebbeles and D. Dorfs, Localized Surface Plasmon Resonances of Various Nickel Sulfide Nanostructures and Au–Ni 3 S 2 Core–Shell Nanoparticles, Chem. Mater., 2017, **29**, 7371–7377.

6 S. Mostafa, F. Behafarid, J. R. Croy, L. K. Ono, L. Li, J. C. Yang, A. I. Frenkel and B. R. Cuenya, Shape-dependent catalytic properties of Pt nanoparticles, J. Am. Chem. Soc., 2010, **132**, 15714–15719.

7 K. Wu and T. Lian, Quantum confined colloidal nanorod heterostructures for solar-to-fuel conversion, Chem. Soc. Rev., 2016, **45**, 3781–3810.

8 M. C. Arno, M. Inam, A. C. Weems, Z. Li, A. L. A. Binch, C. I. Platt, S. M. Richardson, J. A. Hoyland, A. P. Dove and R. K. O'Reilly, Exploiting the role of nanoparticle shape in enhancing hydrogel adhesive and mechanical properties, Nat. Commun., 2020, **11**, 1420.

9 M. A. Halcrow, ed., Spin-crossover materials, John Wiley & Sons Ltd., Chichester, 2013.

10 P. Gütlich and H. A. Goodwin, Spin Crossover in Transition Metal Compounds I, Springer Berlin Heidelberg, Berlin, Heidelberg, 2004.

11 C. Bartual-Murgui, A. Akou, C. Thibault, G. Molnár, C. Vieu, L. Salmon and A. Bousseksou, Spin-crossover metal–organic frameworks: promising materials for designing gas sensors, J. Mater. Chem. C, 2015, **3**, 1277–1285.

12 P. Gütlich and H. A. Goodwin, Spin Crossover in Transition Metal Compounds III, Springer Berlin Heidelberg, Berlin, Heidelberg, 2004.

13 I.-R. Jeon, J. G. Park, C. R. Haney and T. D. Harris, Spin crossover iron(ii) complexes as PARACEST MRI thermometers, Chem. Sci., 2014, **5**, 2461–2465.

14 R. N. Muller, L. Vander Elst and S. Laurent, Spin transition molecular materials: intelligent contrast agents for magnetic resonance imaging, J. Am. Chem. Soc., 2003, **125**, 8405–8407.

15 S. Rat, M. Piedrahita-Bello, L. Salmon, G. Molnár, P. Demont and A. Bousseksou, Coupling Mechanical and Electrical Properties in Spin Crossover Polymer Composites, Adv. Mater., 2018, **30**, 1705275.

16 H. J. Shepherd, I. A. Gural'skiy, C. M. Quintero, S. Tricard, L. Salmon, G. Molnár and A. Bousseksou, Molecular actuators driven by cooperative spin-state switching, Nat. Commun., 2013, **4**, 2607.

17 C. Göbel, C. Hils, M. Drechsler, D. Baabe, A. Greiner, H. Schmalz and B. Weber, Confined Crystallization of Spin-Crossover Nanoparticles in Block-Copolymer Micelles, Angew. Chem. Int. Ed., 2020, **59**, 5765–5770.

18 H. Peng, S. Tricard, G. Félix, G. Molnár, W. Nicolazzi, L. Salmon and A. Bousseksou, Re-Appearance of Cooperativity in Ultra-Small Spin-Crossover [Fe(pz){Ni(CN) 4 }] Nanoparticles, Angew. Chem. Int. Ed., 2014, **53**, 10894–10898.

19 L. Salmon and L. Catala, Spin-crossover nanoparticles and nanocomposite materials, Comptes Rendus Chimie, 2018, **21**, 1230–1269.

20 A. Atitoaie, R. Tanasa and C. Enachescu, Size dependent thermal hysteresis in spin crossover nanoparticles reflected within a Monte Carlo based Ising-like model, J. Magn. Magn. Mater., 2012, **324**, 1596–1600.

21 T. Forestier, S. Mornet, N. Daro, T. Nishihara, S. Mouri, K. Tanaka, O. Fouché, E. Freysz and J.-F. Létard, Nanoparticles of iron(II) spin-crossover, Chem. Commun., 2008, 4327–4329.

22 F. Volatron, L. Catala, E. Rivière, A. Gloter, O. Stéphan and T. Mallah, Spin-Crossover Coordination Nanoparticles, Inorg. Chem., 2008, **47**, 6584–6586.

23 S. Liu, K. Zhou, T. Yuan, W. Lei, H.-Y. Chen, X. Wang and W. Wang, Imaging the Thermal Hysteresis of Single Spin-Crossover Nanoparticles, J. Am. Chem. Soc., 2020, **142**, 15852–15859.

24 D. Mader, S. Pillet, C. Carteret, M.-J. Stébé and J.-L. Blin, Confined Growth of Spin Crossover Nanoparticles in Surfactant-Based Matrices: Enhancing Shape Anisotropy, J. Dispers. Sci. Tech., 2011, **32**, 1771–1779.

25 M. D. Manrique-Juarez, F. Mathieu, V. Shalabaeva, J. Cacheux, S. Rat, L. Nicu, T. Leïchlé, L. Salmon, G. Molnár and A. Bousseksou, A Bistable Microelectromechanical System Actuated by Spin-Crossover Molecules, Angew. Chem. Int. Ed., 2017, **56**, 8074–8078.

26 M. D. Manrique-Juárez, F. Mathieu, A. Laborde, S. Rat, V. Shalabaeva, P. Demont, O. Thomas, L. Salmon, T. Leichle, L. Nicu, G. Molnár and A. Bousseksou, Micromachining-Compatible, Facile Fabrication of Polymer Nanocomposite Spin Crossover Actuators, Adv. Funct. Mater., 2018, **28**, 1801970.

27 D. Hinrichs, R. Himstedt and D. Dorfs, The size-selective interaction of key and lock nanocrystals driven by depletion attraction at the nanoscale, Nanoscale, 2018, **10**, 9899–9907.

28 D. Hinrichs, M. Galchenko, T. Kodanek, S. Naskar, N. C. Bigall and D. Dorfs, Chloride Ion Mediated Synthesis of Metal/Semiconductor Hybrid Nanocrystals, Small, 2016, **12**, 2588–2594.

29 J. H. González-Estefan, M. Gonidec, N. Daro, M. Marchivie and G. Chastanet, Extreme downsizing in the surfactant-free synthesis of spin-crossover nanoparticles in a microfluidic flow-focusing junction, Chem. Commun., 2018, **54**, 8040–8043.

30 B. Weber, Synthesis of Coordination Polymer Nanoparticles using Self-Assembled Block Copolymers as Template, Chem. Eur. J., 2017, **23**, 18093–18100.

31 C. Chen, R. A. L. Wylie, D. Klinger and L. A. Connal, Shape Control of Soft Nanoparticles and Their Assemblies, Chem. Mater., 2017, **29**, 1918–1945.

32 T.-L. Nghiem, D. Coban, S. Tjaberings and A. H. Gröschel, Recent Advances in the Synthesis and Application of Polymer Compartments for Catalysis, Polymers, 2020, **12**. DOI: 10.3390/polym12102190.

33 A. Blanazs, S. P. Armes and A. J. Ryan, Self-Assembled Block Copolymer Aggregates: From Micelles to Vesicles and their Biological Applications, Macromol. Rapid Commun., 2009, **30**, 267–277.

34 Y. Mai and A. Eisenberg, Self-assembly of block copolymers, Chem. Soc. Rev., 2012, **41**, 5969–5985.

35 D. J. Adams and P. D. Topham, in Supramolecular Chemistry, ed. P. A. Gale and J. W. Steed, John Wiley & Sons, Ltd, Chichester, UK, 2012.

36 Y. Lu and M. Ballauff, Spherical polyelectrolyte brushes as nanoreactors for the generation of metallic and oxidic nanoparticles: Synthesis and application in catalysis, Prog. Polym. Sci., 2016, **59**, 86–104.

37 M. Müllner and A. H. Müller, Cylindrical polymer brushes – Anisotropic building blocks, unimolecular templates and particulate nanocarriers, Polymer, 2016, **98**, 389–401.

38 F. H. Schacher, P. A. Rupar and I. Manners, Functional block copolymers: nanostructured materials with emerging applications, Angew. Chem. Int. Ed., 2012, **51**, 7898–7921.

39 U. Tritschler, S. Pearce, J. Gwyther, G. R. Whittell and I. Manners, 50th Anniversary Perspective : Functional Nanoparticles from the Solution Self-Assembly of Block Copolymers, Macromolecules, 2017, **50**, 3439–3463.

40 X. Li, J. Iocozzia, Y. Chen, S. Zhao, X. Cui, W. Wang, H. Yu, S. Lin and Z. Lin, From Precision Synthesis of Block Copolymers to Properties and Applications of Nanoparticles, Angew. Chem. Int. Ed., 2018, **57**, 2046–2070.

41 X. Li, X. Yu, C. Cheng, L. Deng, M. Wang and X. Wang, Electrospun Superhydrophobic Organic/Inorganic Composite Nanofibrous Membranes for Membrane Distillation, ACS Appl. Mater. Interfaces, 2015, **7**, 21919–21930.

42 C. Shao, H.-Y. Kim, J. Gong, B. Ding, D.-R. Lee and S.-J. Park, Fiber mats of poly(vinyl alcohol)/silica composite via electrospinning, Mater. Lett., 2003, **57**, 1579–1584.

43 D. Li and Y. Xia, Direct Fabrication of Composite and Ceramic Hollow Nanofibers by Electrospinning, Nano Lett., 2004, **4**, 933–938.

44 S. Agarwal, A. Greiner and J. H. Wendorff, Functional materials by electrospinning of polymers, Prog. Polym. Sci., 2013, **38**, 963–991.

45 A. Greiner and J. H. Wendorff, Electrospinning: a fascinating method for the preparation of ultrathin fibers, Angew. Chem. Int. Ed., 2007, **46**, 5670–5703.

46 Y. Wang, J. He, H. Chen, J. Chen, R. Zhu, P. Ma, A. Towers, Y. Lin, A. J. Gesquiere, S.-T. Wu and Y. Dong, Ultrastable, Highly Luminescent Organic-Inorganic Perovskite-Polymer Composite Films, Adv. Mater., 2016, **28**, 10710–10717.

47 H. Song and S. Lee, Photoluminescent (CdSe)ZnS quantum dot–polymethylmethacrylate polymer composite thin films in the visible spectral range, Nanotechnology, 2007, **18**, 55402.

48 J. Laisney, D. Morineau, C. Enachescu, R. Tanasa, E. Rivière, R. Guillot and M.-L. Boillot, Mechanical-tuning of the cooperativity of SC particles via the matrix crystallization and related size effects, J. Mater. Chem. C, 2020, **8**, 7067–7078.

49 Y. Raza, F. Volatron, S. Moldovan, O. Ersen, V. Huc, C. Martini, F. Brisset, A. Gloter, O. Stephan, A. Bousseksou, L. Catala and T. Mallah, Matrix-dependent cooperativity in spin crossover Fe(pyrazine)Pt(CN)4 nanoparticles, Chem. Commun, 2011, **47**, 11501–11503.

50 R. Torres-Cavanillas, R. Sanchis-Gual, J. Dugay, M. Coronado-Puchau, M. Giménez-Marqués and E. Coronado, Design of Bistable Gold@Spin-Crossover Core-Shell Nanoparticles Showing Large Electrical Responses for the Spin Switching, Adv. Mater., 2019, **31**, e1900039.

51 M. Palluel, N. M. Tran, N. Daro, S. Buffière, S. Mornet, E. Freysz and G. Chastanet, The Interplay between Surface Plasmon Resonance and Switching Properties in Gold@Spin Crossover Nanocomposites, Adv. Funct. Mater., 2020, **30**, 2000447.

52 O. Klimm, C. Göbel, S. Rosenfeldt, F. Puchtler, N. Miyajima, K. Marquardt, M. Drechsler, J. Breu, S. Förster and B. Weber, Synthesis of Fe(L)(bipy)n spin crossover nanoparticles using blockcopolymer micelles, Nanoscale, 2016, **8**, 19058–19065.

53 C. Göbel, O. Klimm, F. Puchtler, S. Rosenfeldt, S. Förster and B. Weber, Synthesis of Fe(Leq)(Lax) n coordination polymer nanoparticles using blockcopolymer micelles, Beilstein J. Nanotechnol., 2017, **8**, 1318–1327.

54 C. Göbel, G. Hörner, A. Greiner, H. Schmalz and B. Weber, Synthesis of Zn-based 1D and 2D coordination polymer nanoparticles in block copolymer micelles, Nanoscale Adv., 2020, **2**, 4557–4565.

55 S. O'Driscoll, G. Demirel, R. A. Farrell, T. G. Fitzgerald, C. O'Mahony, J. D. Holmes and M. A. Morris, The morphology and structure of PS-b-P4VP block copolymer films by solvent annealing: effect of the solvent parameter, Polym. Adv. Technol., 2011, **22**, 915–923.

56 T. H. Kim, J. Huh, J. Hwang, H.-C. Kim, S. H. Kim, B.-H. Sohn and C. Park, Ordered Arrays of PS- b -P4VP Micelles by Fusion and Fission Process upon Solvent Annealing, Macromolecules, 2009, **42**, 6688–6697.

57 S. Förster, M. Zisenis, E. Wenz and M. Antonietti, Micellization of strongly segregated block copolymers, J. Chem. Phys., 1996, **104**, 9956–9970.

58 H. Cho, H. Park, S. Park, H. Choi, H. Huang and T. Chang, Development of various PS-b-P4VP micellar morphologies: fabrication of inorganic nanostructures from micellar templates, J. Colloid Interface Sci., 2011, **356**, 1–7.

59 N. Ali and S.-Y. Park, Micellar structures of poly(styrene-b-4-vinylpyridine)s in THF/toluene mixtures and their functionalization with gold, Langmuir, 2008, **24**, 9279–9285.

60 I. I. Perepichka, Q. Lu, A. Badia and C. G. Bazuin, Understanding and controlling morphology formation in Langmuir-Blodgett block copolymer films using PS-P4VP and PS-P4VP/PDP, Langmuir, 2013, **29**, 4502–4519.

61 L. Song, Y. M. Lam, C. Boothroyd and P. W. Teo, One-step synthesis of titania nanoparticles from PS-P4VP diblock copolymer solution, Nanotechnology, 2007, **18**, 135605.

62 S. Roland, D. Gaspard, R. E. Prud'homme and C. G. Bazuin, Morphology Evolution in Slowly Dip-Coated Supramolecular PS- b -P4VP Thin Films, Macromolecules, 2012, **45**, 5463–5476.

63 J. N. Israelachvili, Intermolecular and Surface Forces, Elsevier, Amsterdam, 2011.

64 A. Walther, A. S. Goldmann, R. S. Yelamanchili, M. Drechsler, H. Schmalz, A. Eisenberg and A. H. E. Müller, Multiple Morphologies, Phase Transitions, and Cross-Linking of Crew-Cut Aggregates of Polybutadiene- block -poly(2-vinylpyridine) Diblock Copolymers, Macromolecules, 2008, **41**, 3254–3260.

65 B. Weber, E. S. Kaps, C. Desplanches and J.-F. Létard, Quenching the Hysteresis in Single Crystals of a 1D Chain Iron(II) Spin Crossover Complex, Eur. J. Inorg. Chem., 2008, **2008**, 2963–2966.

66 B. Weber, R. Tandon and D. Himsl, Synthesis, Magnetic Properties and X-ray Structure Analysis of a 1-D Chain Iron(II) Spin Crossover Complex with wide Hysteresis, Z. Anorg. Allg. Chem., 2007, **633**, 1159–1162.

67 B. Weber, Mössbauer spectra of FeII spin crossover complexes with N2O4 coordination sphere, Möss. Eff. Ref. Data J., 2012, **35**, 238–254.

68 J. Weihermüller, S. Schlamp, B. Dittrich and B. Weber, Kinetic Trapping Effects in Amphiphilic Iron(II) Spin Crossover Compounds, Inorg. Chem., 2019, **58**, 1278–1289.

69 S. Schönfeld, C. Lochenie, P. Thoma and B. Weber, 1D iron(ii) spin crossover coordination polymers with 3,3′-azopyridine – kinetic trapping effects and spin transition above room temperature, CrystEngComm, 2015, **17**, 5389–5395.

70 E.-G. Jäger, E. Häussler, M. Rudolph and A. Schneider, Struktur-Reaktivitts-Beziehungen bei koordinativ-ungesttigten Chelatkomplexen. VI. Synthese, Adduktbildung, Redoxpotentiale und photochrome lodderivate von Eisen(II)-Komplexen Schiffscher Basen mit elektronenziehenden Substituenten, Z. Anorg. Allg. Chem., 1985, **525**, 67–85.

71 K. Lagarec and D. G. Rancourt, Recoil, mössbauer spectral analysis software for windows 1.0, Department of Physics, University of Ottawa, Canada, 1998.

72 R. A. Brand, WinNormos-for-Igor, 2009.

73 S. K. Varshney, X. F. Zhong and A. Eisenberg, Anionic homopolymerization and block copolymerization of 4-vinylpyridine and its investigation by high-temperature size-exclusion chromatography in N-methyl-2-pyrrolidinone, Macromolecules, 1993, **26**, 701–706.